Published in IET Microwaves, Antennas & Propagation
Received on 18th January 2008
Revised on 9th March 2008
doi: 10.1049/iet-map:20080015

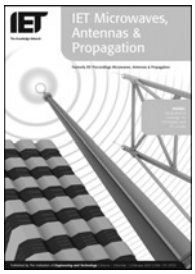

ISSN 1751-8725

Bandwidth-dependent modelling of small-scale fade depth in wireless channels

W.Q. Malik[1] *B. Allen*[2] *D.J. Edwards*[2]

[1]*Department of Brain and Cognitive Sciences, Massachusetts Institute of Technology, 77 Massachusetts Avenue, Cambridge, MA 02139, USA*
[2]*Department of Engineering Science, University of Oxford, Parks Road, Oxford OX1 3PJ, UK*
E-mail: wqm@mit.edu

Abstract: In this paper, the relation between small-scale fade depth and channel bandwidth in an indoor environment is investigated. The fade depth, a measure of the signal power variability over a local region in space, is evaluated for narrowband, wideband and ultrawide-band channels. The experimental analysis is based on frequency-domain measurements in the 3.1–10.6 GHz microwave band. Physical insight into the fading process is provided, and the effect of increasing bandwidth and temporal resolution is discussed. A dual-slope empirical model is developed, which accurately describes the relationship between fade depth and channel bandwidth. It is demonstrated that the fade depth, considered at the three standard deviation values, converges to about 4 dB at 1 GHz bandwidth, and a further increase in bandwidth yields only a marginal improvement in fade mitigation.

1 Introduction

Multipath propagation in wireless channels can cause destructive signal interference and lead to small-scale fading [1]. A channel with unresolved multipath components (MPCs) can suffer from severe fading, leading to a high system outage probability. Fading is closely related to the temporal or spatial variability of the channel. The variation of the statistical properties of fading processes according to the propagation conditions is well understood and recognised in the various radio communications standards.

In a narrowband outdoor mobile channel without line-of-sight (LOS) between transmitter and receiver, such as a microcellular environment modelled as a ring of scatterers around the receiver, the fading coefficient amplitudes follow the Rayleigh distribution [2]. Dense clutter, such as that encountered in ground-probing and marine radar channels, leads to Weibull-distributed channel coefficients [3]. Severely faded channels can also be well modelled with Student's t distribution [4]. For wideband channels, the fading coefficients refer to the tap amplitudes in the tapped delay line, where each tap represents the composite contribution of the incident MPCs within a resolvable time-bin. The coefficients of ultrawide-band (UWB) fading channel [5] are sometimes modelled by the Nakagami-m, Weibull or lognormal distributions [6–8]. Correspondingly, the narrowband channel energy follows the chi-square distribution, whereas the wideband tap energy follows the Gamma distribution. Finally, the total wideband channel energy, obtained as the sum of the individual tap energies, follows the lognormal distribution [6].

The above studies reveal significant differences in the statistical behaviour of the radio channel as a result of variation in its bandwidth. Some other works have analysed the impact of bandwidth on channel fading using techniques such as eigenanalysis. The number of significant eigenvalues of the channel covariance matrix, obtained from the channel impulse response, was shown to scale linearly with bandwidth in [9], while Hayer *et al.* [10] reported that a saturation point is reached at a certain bandwidth. These results indicate an increase in the stochastic degrees of freedom with bandwidth in frequency-selective channels, leading to reduced fading.

In this paper, we investigate the variation of wideband channel energy with bandwidth over the UWB spectral

range. The mean energy and fade depth are important channel parameters from the perspective of system design, as they affect the probability of outage [1, 11]. In this work, the fade depth refers to the variation of the received symbol energy about its local mean due to small-scale fading. The fade depth determines the required fade margin and link budget for acceptably low system outage probability [11]. Owing to the central importance of this quantity in radio network planning, a number of fade depth prediction models have been presented. Cardoso and Correia used simulated radio channels centred at 60 GHz to relate the fade depth to the propagation conditions characterised by the Rice factor K and equivalent bandwidth [12]. According to that study, the fade depth falls monotonically with the equivalent bandwidth, while the variation of fade depth with bandwidth increases as the LOS component becomes weak and K decreases. The Olsen-Segal fade depth prediction model [13], adopted by ITU-R for terrestrial point-to-point LOS links, is an empirical extension of the Barnett model [14]. In the context of wideband code-division multiple access (CDMA) antenna diversity systems, Wilson *et al.* studied the impact of bandwidth on fade depth for up to 10 MHz wide channels [15].

In a narrowband channel, the fade depth can be as large as 30 dB [16], while the UWB fade depth is much lower, that is, up to ~5 dB for a 1 GHz wide signal [17]. Although these and other works have analysed the fade depth at a given bandwidth, there is no information on the relationship between fade depth and channel bandwidth. Such characterisation is especially important for practical UWB systems, as it would allow the system designer to determine the optimal operating bandwidth with the required level of performance–complexity tradeoff. The unavailability of this information can be partly attributed to the fact that channel measurements over a very large bandwidth are generally difficult due to practical limitations, as highlighted in [6]. Indeed, Molisch [6] notes that very few sets of measurement data are available at present that span the entire indoor UWB bandwidth (3.1–10.6 GHz) allocated by the Federal Communications Commission (FCC) [18].

The main contribution of this paper is a simple empirical fade depth model applicable universally to narrowband, wideband and UWB indoor channels. The propagation scenarios consider both LOS and non-line-of-sight (NLOS) propagation. The effect of polarisation is investigated by analysing both vertical and horizontal link polarisations according to the transmitting and receiving antenna orientations. The rest of this paper is organised as follows. Section 2 describes the channel model and measurement procedure. Section 3 presents the methodology for the evaluation of fade depth and discusses its relation with bandwidth as observed from the data. Section 4 presents a model that captures this dependence of fade depth on bandwidth. Finally, Section 5 concludes the paper.

2 Channel model and measurement

In this paper, we restrict our attention to the indoor propagation channel encountered by wireless local (WLAN) and personal area network (WPAN) applications. Such an environment, especially in an office setting and with wideband signals, is generally considered to be temporally quasi-static because of practical limitations on mobility [19]. This section presents the channel model used in this paper and the channel measurement methodology for the subsequent analysis.

2.1 Channel model

We consider the tapped delay line model to represent the frequency-selective channel, which includes the physical propagation channel and the transmitting and receiving antennas [20]. The complex impulse response (CIR) of the N–tap wideband channel is given by

$$h(\tau) = \sum_{n=0}^{N-1} a_n e^{j\theta_n} \delta(\tau - n\Delta\tau) \tag{1}$$

where a_n and θ_n represent the amplitude and phase of the nth timebin, τ the time delay with respect to the first resolved MPC, $\Delta\tau = 1/W$ the width of the resolvable timebin, W the channel bandwidth, $N = \lceil \tau_{\max}/\Delta\tau \rceil$ is the number of timebins in $h(\tau)$, $\tau_{\max}$ is the maximum excess delay and $\delta(.)$ the Kronecker delta function[1]. If the nth timebin does not contain any MPC, we have $a_n = 0$. The CIR is related to the channel transfer function (CTF) through the discrete Fourier transform. The baseband CTF is represented by

$$\begin{aligned} H(f) &= \mathcal{F}\{h(\tau)\} = \int_{-\infty}^{\infty} h(\tau)\, e^{-j2\pi f\tau}\, d\tau \\ &= \sum_{k=0}^{N_f-1} \alpha_k e^{j\phi_k} \delta(f - k\Delta f) \end{aligned} \tag{2}$$

where α_k and ϕ_k are the magnitude and phase responses of the channel at the kth frequency point, N_f the number of frequency points in the CTF, $\Delta f = W/(N_f - 1)$ is the frequency resolution and $\mathcal{F}\{.\}$ the discrete Fourier transform operation. From the Parseval relation, the wideband channel energy is

$$E_h = \int_0^{\tau_{\max}} |h(\tau)|^2 d\tau = \int_W |H(f)|^2 df. \tag{3}$$

2.2 Measurement environment

Indoor channel measurements are conducted in two small office rooms with dimensions $6 \times 6\,m^2$ and $5.7 \times 5\,m^2$, respectively, as shown in Fig. 1. Each room presents a dense scattering environment, as it contains various metallic objects such as computers, cabinets, furniture and lab equipment (Fig. 2).

doi: 10.1049/iet-map:20080015

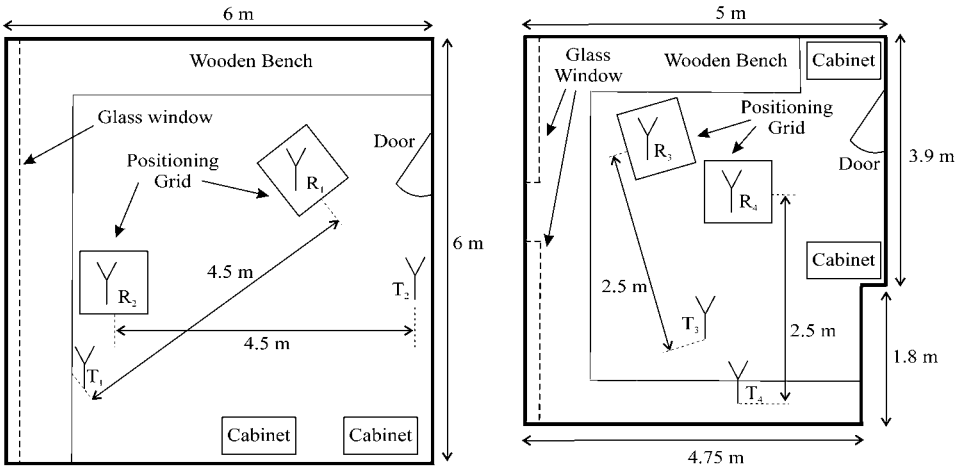

Figure 1 *Indoor propagation environment and measurement configuration*
Measured links are defined by the T_iR_i antenna pair, $i = 1 \ldots, 4$

Within each room, measurements are performed at two different sets of locations, so that a total of four sets of small-scale measurements are obtained. The corresponding locations of the transmitter–receiver pairs are represented in Fig. 1 by T_i and R_i where $i = 1, \ldots, 4$. For the ith location in the dataset, the position of the transmitting antenna is fixed, whereas the receiving antenna is placed at $N_i = 900$ separate position within a $1\ \mathrm{m}^2$ area. These positions are controlled by an automated positioning grid, shown in Fig. 3. The successive positions are chosen to be 0.03 m apart to allow sufficient decorrelation. This spacing is of the same order as that used in some of the previous grid-based small-scale channel measurements, such as [8, 21, 22]. Thus 900 channel responses are collected in the ith measurement dataset for a single-grid location, so that the full ensemble of measured realisations, denoted by $\mathcal{R}$, comprises $R = 3600$ individual UWB channel responses.

In the rest of this paper, the CTF at the jth position within the ith grid dataset is denoted by $H(i, j, f)$. Accordingly, we have the CIR $h(i, j, \tau)$, the time-domain tap amplitude $a_n(i, j)$, the frequency-domain amplitude $\alpha_k(i, j)$ and the channel energy $E_h(i, j)$. The spatial or temporal variability of the radio channel introduces randomness so that the channel response and energy can be treated as stochastic quantities. In this paper, we do not make any assumptions about the distribution of the tap amplitudes or related quantities.

As a consequence of the regulatory constraints on UWB emissions [18], the range of high-rate UWB communications systems is limited to only a few metres [23]. It is therefore considered appropriate in this study to restrict the measurements to within small-sized office rooms. The distance between the transmitting antenna and

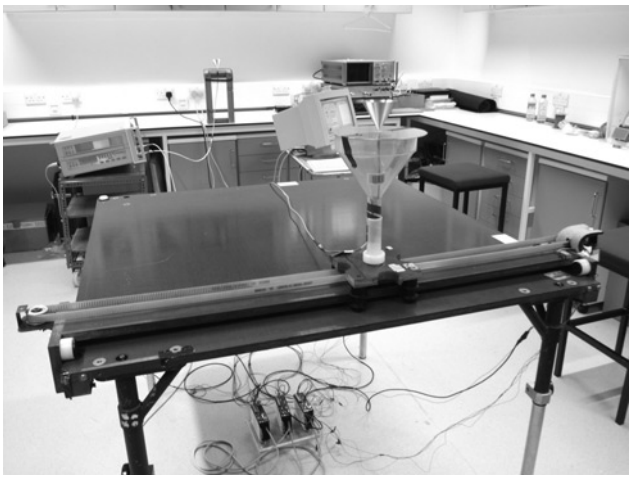

Figure 2 *Channel measurement apparatus including the positioning grid, the discone antennas, the vector network analyser and the data-logging computer*

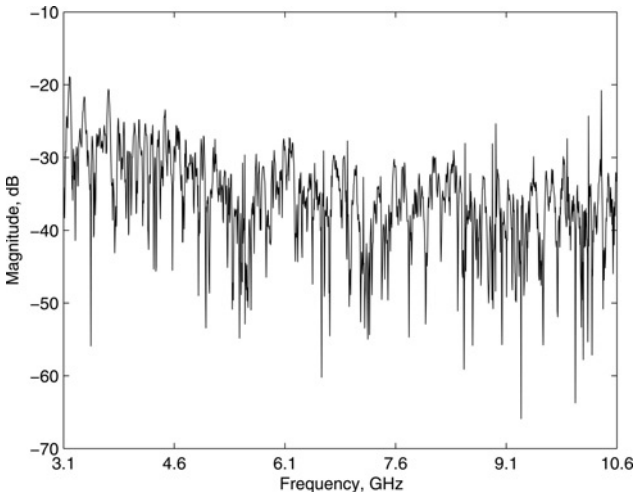

Figure 3 *Measured UWB channel transfer function over the FCC band, 3.1–10.6 GHz, as an example*

the centre of the grid is 4.5 m in the first room and 2.5 m in the second room. The transmitting and receiving antennas are placed at the same height of 1.5 m.

These measurements are undertaken for both LOS and NLOS propagation scenarios. A large block of RF-absorbing material, similar to that used in anechoic chambers, is placed between the transmitting and receiving antennas for creating the NLOS scenario and investigating the effect of shadowing. The propagation environment is physically isolated during the measurement.

An important and unique aspect of this study is the effect of signal polarisation on fade depth. For this purpose, the transmitting and receiving antennas are placed vertically to measure the vertically polarised (V) link. For the measurement of the horizontally polarised (H) link, the antennas are rotated by 90° so that the antenna axis still remains perpendicular to the Poynting vector corresponding to the direct path. In this paper, we restrict our attention to co-polarised V and H links, and the cross-polarized links are left for future investigation.

2.3 Channel sounding

Channel measurements are conducted using the swept frequency channel sounding approach with the help of an HP8722 vector network analyser (VNA). The transmission parameter, $S_{21}(f)$, of the scattering matrix, $\boldsymbol{S}(f)$, is measured over the frequency range of interest. The FCC-allocated UWB spectrum is chosen for this purpose, and therefore the channel is sounded between $f_l = 3.1$ GHz and $f_h = 10.6$ GHz. This bandwidth is swept at $N_\mathrm{f} = 1601$ discrete frequency points, ensuring that the frequency sampling, $\Delta f = 4.6875$ MHz, is sufficiently dense to meet the Nyquist criterion, that is, we have $\Delta f < W_\mathrm{c} \simeq 30$ MHz, where W_c is the coherence bandwidth of the channel.

A wideband low-noise amplifier (LNA) with 30 dB gain is connected between the receiving antenna and the VNA. RF cables with a low loss specification of up to a maximum of 6 dB over the band of interest are used. Omni-directional UWB antennas, with the discone construction as described in detail in [24], are deployed at both ends of the link. End-to-end calibration of the measurement system is performed by removing the antennas and connecting the cable ends, including the LNA. Complex frequency-domain compensation is applied to the measured channel responses using the calibration data during the post-processing stage in order to remove the attenuation and phase distortion of the cables, connectors and LNA.

As a representative example, the CTF measured at the center of the grid in the T_1R_1 dataset is shown in Fig. 3. For the ith measurement dataset in Fig. 1, the local mean pathloss is removed from each channel response within that dataset. To this end, the pathloss normalisation factor, L_i, for the ith dataset is calculated as the root mean channel energy, that is

$$L_i = \sqrt{\frac{1}{N_i}\sum_{j=1}^{N_i} E_b(i,j)} \tag{4}$$

The jth CTF in the ith dataset is then divided by L_i to remove the mean pathloss from the measurement ensemble.

3 Evaluation of fade depth

In this section, we investigate the variation of fade depth with bandwidth. The comparative analysis is undertaken for narrowband, wideband and UWB channels over a range of bandwidths. The transfer function, $H_\mathrm{b}(i,j,f)$, of the filtered channel with bandwidth W_b, is obtained from $H(i,j,f)$ by considering the appropriate number of measured frequency points, $n_\mathrm{f} = 1, \ldots, N_\mathrm{f}$. Thus the channel bandwidth, $W_\mathrm{b} = n_\mathrm{f}\Delta f$, varies in our case from an arbitrarily small value for a pure sinusoid to 7.5 GHz for a full-band UWB signal. The centre frequency is maintained at $f_\mathrm{c} = (f_l + f_h)/2 = 6.85$ GHz for a fair comparison, and the discrete centre frequency sample index is denoted by n_c. The bandwidth is altered by including $n = (n_\mathrm{f} - 1)/2$ measured frequency points symmetrically distributed on either side of n_c, assuming odd n_f without loss of generality. Then the band-limited CTF is given by

$$H_\mathrm{b}(i,j,f) = \begin{cases} H(i,j,f), & \text{if } |f - f_\mathrm{c}| \le W_\mathrm{b}/2 \\ 0, & \text{otherwise} \end{cases} \tag{5}$$

As the measurement data are obtained in the frequency domain, the following fade depth analysis is also undertaken in the same domain in order to prevent the inaccuracy arising from transformation, such as the energy leakage across timebins or loss of time resolution due to windowing. By the Parseval relation, this frequency-domain energy integration is equivalent to optimal multipath energy integration using a maximal-ratio combining (MRC) rake receiver or all-rake. The results therefore hold directly for rake-based wideband techniques such as direct-sequence spread-spectrum or time-hopping impulse radio. Similarly, our technique and its results are also valid for energy detection and orthogonal frequency-division multiplexing (OFDM) schemes [25].

3.1 Mean channel energy

The energy of the band-limited CTF, $H_\mathrm{b}(i,j,f)$, integrated across the frequency band is given by

$$p_\mathrm{b}(i,j) = \sum_{k=n_\mathrm{c}-n}^{n_\mathrm{c}+n} |\alpha_k(i,j)|^2 \tag{6}$$

An increase in the channel bandwidth beyond the coherence bandwidth implies an increase in the stochastic degrees of freedom in the frequency domain, and can thus provide

doi: 10.1049/iet-map:20080015

frequency diversity. In particular, the energy integration in (6) across frequency samples, some of which fade independently, indicates frequency diversity with MRC [11].

The energy, p_b, for each W_b is averaged across the measurement locations to obtain the mean statistics. Fig. 4 shows the variation of the spatially averaged channel energy, in decibel scale, as a function of bandwidth for the NLOS V channel. The bandwidth–energy curve depicts a linear relationship on a log–log plot, as predicted from the frequency diversity explanation above. Note that, strictly speaking, $W_b = 0$ when $n = 0$. Since $\lim_{W_b \to 0} \log_{10} W_b = -\infty$, the effective bandwidth, $W_b = \Delta f$, is substituted in that particular case for mathematical convenience. In other words, the bandwidth of the narrowband signal is substituted by the smallest measurable bandwidth from our measurement system. This allows the inclusion of the single centre-frequency sample point, n_c, in the log-bandwidth plot. There is no loss of generality since, as discussed in Section 2, $\Delta f \ll W_c$, and therefore the fading at n_c is flat over Δf.

This result also indicates that the mean channel energy per unit bandwidth, p_b/W_b, remains constant when the bandwidth increases symmetrically about f_c. For vertically polarised indoor channels, the power spectral density of the channel is dominated by the $1/f^2$ Friis behaviour due to the omnidirectional antennas. With an increase in the bandwidth, the increase in p_b/W_b in the $f = [f_c - W_b/2, f_c]$ region is balanced by its decrease in the $f = [f_c, f_c + W_b/2]$ region.

3.2 Fade depth estimation

For the indoor multipath channel, the fade depth is a measure of the variation in the channel energy due to small-scale fading. In outdoor environments, the temporal variability of the channel also causes fading, but our current treatment is limited to spatial fading only. The justification for this lies in the fact that the indoor channel does not suffer from large temporal variations because of the reasonable assumption of limited mobility of the transceivers and scatterers. The temporal variability is further reduced when the bandwidth is very wide, since the Doppler spread due to a slow moving object is insignificant compared with the channel bandwidth. The fade depth is defined as the observed range of signal power variation. Statistically, the fade depth is related to the standard deviation, σ, of the channel energy expressed in decibel scale. Mathematically

$$F_{s\sigma} = s\sqrt{\frac{1}{R}\sum_{r\in R}(\rho_r - \bar{\rho})^2} \tag{7}$$

where $\rho_r = 10\log_{10} p_b(i,j)$ is the channel energy in decibels for the rth realisation with position index (i,j) in the measurement dataset, and $\bar{\rho} = 1/R\sum_{r\in\mathcal{R}} \rho_r$. In order to cover a range of system performance levels, the fade depth is defined in (7) at the σ, 2σ, 3σ and 6σ levels, denoted by $F_{s\sigma}$, where $s = 1, 2, 3, 6$.

The fade depths are estimated in this manner for a variety of channel bandwidths. As shown in Fig. 5 for the NLOS V channel, it is observed that $F_{s\sigma} = 5.7, 11.3, 17.0, 34.0$ dB at $s = 1, 2, 3, 6$, respectively, at $W_b = \Delta f$. On the other hand, we observe $F_{s\sigma} = 1.0, 1.9, 2.9, 5.8$ dB at $s = 1, 2, 3, 6$, respectively, with $W_b = 7.5$ GHz. A comparison of the corresponding values shows that the transition from the narrowband to the UWB channel leads to an approximately six-fold reduction in fade depth. Thus clearly W_b has a very significant impact on $F_{s\sigma}$.

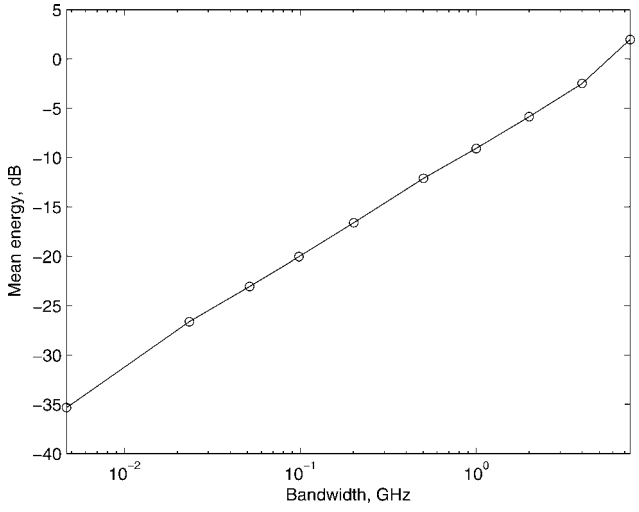

Figure 4 *Received signal energy after local mean pathloss normalisation, averaged across the measurement ensemble, as a function of the channel bandwidth with the center frequency kept constant*

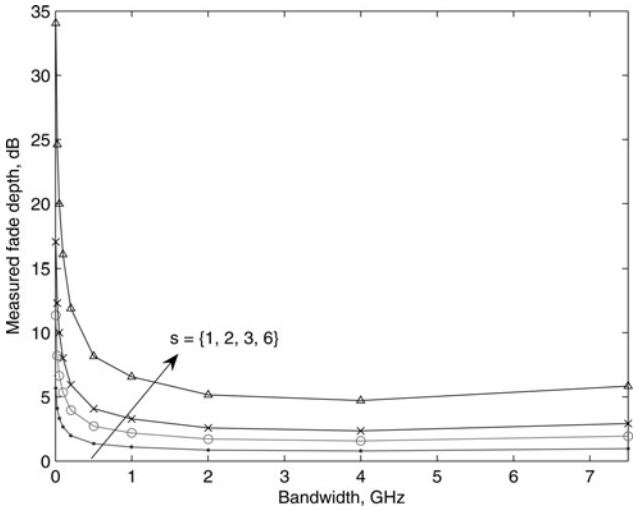

Figure 5 *Measured fade depth, $F_{s\sigma}$, as a function of channel bandwidth for various values of s*

The $F_{s\sigma}$ curves appear to converge to their asymptotic values at ~1 GHz, which is in agreement with the results in [26]. A further increase in W_b yields only a minor reduction in $F_{s\sigma}$, and no performance improvement with larger W_b can be expected once the fade margin reaches a constant value. The saturation of the multipath resolution capability of wideband systems has also been reported in [10, 27].

These observations indicate that the additional resilience to fading from bandwidths beyond ~1 GHz is insignificant. However, a further increase in bandwidth beyond this critical point may still continue to improve the spatial resolution important for localisation and imaging systems [5].

3.3 Physical insight

The channel energy, p_b, is now renormalised with respect to the mean of the spatial ensemble defined by the entire set of measurement points to remove the bias from the energy probability distribution. Its CDF is then estimated, as shown in Fig. 6. It is observed that the CDFs become progressively steeper with bandwidth, indicating the decreasing spread of the fading process. The tightening of the channel energy distribution, however, appears to be nonlinear in W_b, as can also be inferred from Fig. 5. The results shown in Fig. 6 are obtained from the V NLOS channel data, and the other types of channels exhibit a similar behaviour. This effect provides the basis for the tightening of the probability density function of wideband channel capacity with an increase in the channel bandwidth, as found in [28–30].

Time-domain analysis is insightful in understanding the physical reasoning behind the dependence of $F_{s\sigma}$ on W_b. The band-limited CIRs corresponding to the frequency subchannels obtained from the CTF of Fig. 3*a* for various W_b are shown in Fig. 7. The CTF under consideration is measured at the centre of the grid in scenario T_1R_1 with

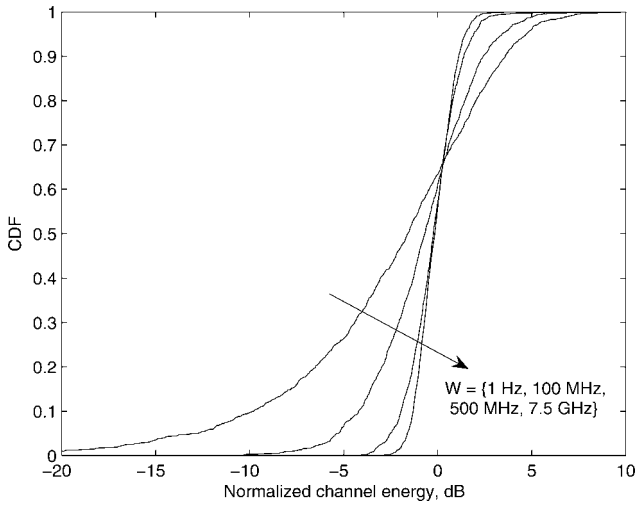

Figure 6 *CDFs of the mean-normalised channel energy for various values of the channel bandwidth, W*

LOS propagation, so that the transmitter–receiver separation is 4.5 m. The actual propagation delay of the direct signal component is therefore 15 ns. In the CIR, the propagation delay corresponds to the first peak. From Fig. 7*a*, the estimated propagation delay for a bandwidth of 100 MHz is, however, 17.9 ns, which is an error of 17%. As the bandwidth increases in Fig. 7, the first composite MPC decomposes into multiple components. Thus at $W_b = 500$ MHz, a CIR local maximum is detected at 15.6 ns. However, the first resolvable MPC is over 10 dB lower in magnitude than the next, which is now the strongest, as a result of multipath fading. With further increase in bandwidth, greater multipath resolution is obtained and the time-of-arrival estimate for the direct path becomes progressively more accurate. Similar observations can be made for the other paths. In addition, the interpath interference is reduced, resulting in the first detectable MPC correctly achieving the strongest amplitude at very large bandwidth. These results are consistent with the UWB CIR analysis in [31]. Also, it can be observed that the number of resolved paths continues to increase with W_b, on account of the specular paths that dominate the wideband channel response in typical indoor propagation environments.

3.4 Statistical explanation

In a narrowband multipath channel, a significant number of MPCs may appear in the same time-bin, leading to Rayleigh or Rician distributed amplitude statistics on account of the central limit theorem [2]. However, when the bandwidth increases, the likelihood that a single resolvable time-bin contains multiple mutually interfering MPCs decreases progressively, with perfect multipath orthogonality in the infinite bandwidth limit. This effect explains the statistical phenomenon that is the dominant contributor to the reduction of fade depth with increasing bandwidth.

Consider a set of independent and identically distributed (i.i.d.) complex random variables, x_i, $i = 1, \ldots, L$, that represent the complex amplitudes of the L incident MPCs. For a narrowband channel with vanishing bandwidth, that is, $W \to 0$, and consequently no multipath resolution, the SNR is given by $\gamma_{NB} = \left|\sum_{i=1}^{L} x_i\right|^2$. On the other hand, for a UWB channel with all MPCs resolved, the output signal power of an MRC rake is $\gamma_{\mathrm{UWB}} = \sum_{i=1}^{L} |x_i|^2$. Now if $|x_1| = \cdots = |x_L|$ and $\angle x_i \sim U[-\pi, \pi]$, it follows from the triangle inequality that $\gamma_{\mathrm{UWB}} \geq \gamma_{NB}$ in a multipath channel.

If X_k represent the frequency-domain channel coefficients, a single coefficient X_c is narrowband, and therefore Rayleigh distributed, as is well established for conventional narrowband channels with dense scattering [11]. Then $\gamma_{NB} = |X_c|^2$ follows the chi-square distribution. The energy of a wideband channel with K such coefficients is $\gamma_{\mathrm{UWB}} = \sum_{i=1}^{K} |X_k|^2$, computed in the frequency domain

doi: 10.1049/iet-map:20080015

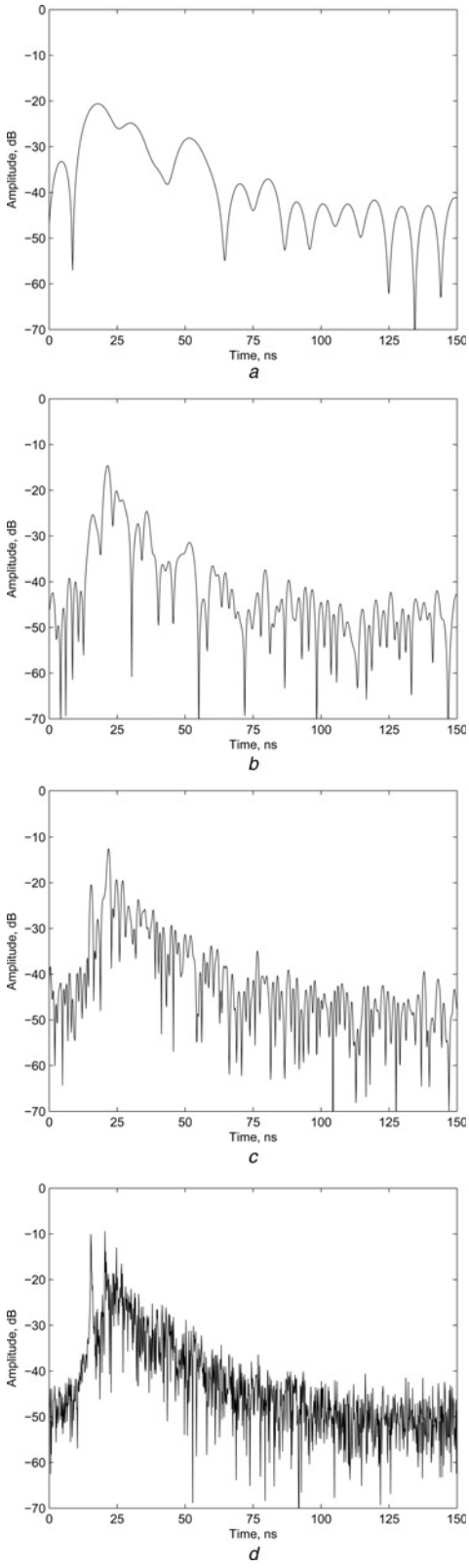

Figure 7 *The band-limited channel impulse responses, normalised to the root energy, extracted from the LOS frequency transfer function in Fig. 2a, with centre frequency 6.85 GHz and the specified bandwidth*

a 100 MHz
b 500 MHz
c 1 GHz
d 7.5 GHz

from (5). From the central limit theorem, as $K \to \infty$ or $W \to \infty$, γ_{UWB} converges to a normal distribution with lower variance than that of γ_{NB}.

4 Fade depth model

A simple empirical model for the estimation of fade depth as a function of channel bandwidth is now proposed. Fig. 8 shows the measured fade depth, evaluated earlier in Section 3, plotted against the bandwidth on a logarithmic scale. The observation of the break point occurring at $W_0 = 1$ GHz is confirmed from this plot, and intuitively a dual-slope regression fit is therefore appropriate. Note that a better approximation may be obtained with a higher-order polynomial, but we use a dual-slope model in the interest of simplicity and intuitiveness, and demonstrate that the simpler model also yields a good approximation. A slope-constant model is adopted as a further simplification in this paper, given by the piecewise regression

$$F_{s\sigma} = \begin{cases} s(k_1 - k_2 \log_{10} W_{\mathrm{b}}), & \text{if } W_{\mathrm{b}} < W_0 \\ sk_3, & \text{otherwise} \end{cases} \tag{8}$$

where $s = 1, 2, 3, 6$ denotes the number of standard deviations considered, W_0 the breakpoint and k_i, $i = 1, \ldots, 3$, the model parameters. Alternatively, a linear scale representation of the model can be obtained as

$$F'_{s\sigma} = \begin{cases} 10^{sk_1} W_{\mathrm{b}}^{-sk_2}, & \text{if } W_{\mathrm{b}} < W_0 \\ 10^{sk_3}, & \text{otherwise} \end{cases} \tag{9}$$

where $F'_{s\sigma}$ is the fade depth in linear scale. The parameters k_1 and k_2, for the linear region, $W_{\mathrm{b}} \leq W_0$, are obtained as the intercept and slope of the regression line defined by

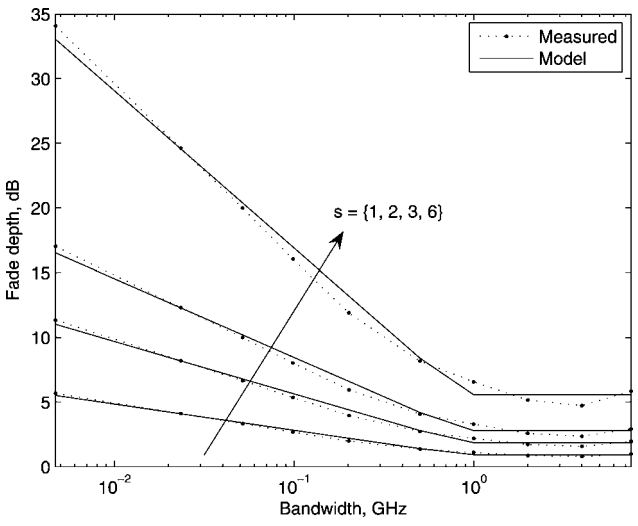

Figure 8 *Dual-slope model for the fade depth, $F_{s\sigma}$, for various values of s*

Measured fade depth is also shown for comparison

Table 1 Empirical fade depth model parameters

Parameters	Vertical polarisation		Horizontal polarisation	
	LOS	NLOS	LOS	NLOS
k_1	5.65	6.34	7.09	5.75
k_2	1.72	2.02	2.20	1.80
k_3	1.41	0.93	1.68	1.14

$\log_{10} W_b$ against $F_{s\sigma}$. Thus from (8), we have

$$k_1 = \frac{F_{s\sigma}}{s}\Big|_{W_b \to 1} \tag{10}$$

and

$$k_2 = \frac{sk_1 - F_{s\sigma}}{s \log_{10} W_b} \tag{11}$$

The fade depth at bandwidth beyond the break-point, W_0, of the model is characterised by the third parameter of the model, k_3, obtained as the mean fade depth at large bandwidth, that is,

$$k_3 = \frac{1}{n_i} \sum_{i=1}^{n_i} \frac{F_{s\sigma}}{s}\Big|_{n_f \geq n_0} \tag{12}$$

where n_0 represents the number of frequency points corresponding to $W_b \simeq W_0$ and n_i is the number of fade depth values used in the estimation for such wideband channels with bandwidth larger than W_0.

The values of the three parameters, obtained empirically for a variety of propagation channel types, are listed in Table 1. An inspection of Table 1 reveals that the intercept parameter, k_1, is somewhat larger in NLOS V and LOS H channels compared with the LOS V and NLOS H channels. A larger value of the intercept implies a greater fade depth and consequent power loss at the receiver when the channel bandwidth is vanishingly small. Thus, from Table 1, an indoor narrowband system, with $W_b \to 1$ Hz and vertical polarisation, will experience $F_\sigma = 17$ and 19 dB when operated in LOS and NLOS conditions, respectively. As W_b increases, the values of F_σ for various signal polarisations and propagation converge, in accordance with (8). Furthermore, the difference between the values of the slope parameter, k_2 is relatively small, as observed from Table 1. The asymptotic large-bandwidth fade depth parameter, k_3, varies by <1 dB for the various propagation conditions in Table 1. On the basis of these observations, we can infer that the fade depth in the measured indoor environments is nearly independent of the signal polarization and LOS conditions, especially for the case of wideband and UWB channels.

Fig. 8 shows close agreement between the measurement and model for the fade depth of the NLOS V channel. The model error at W_0 is 0.5 dB for $F_{3\sigma}$ and lower for smaller s. The model error for $F_{3\sigma}$ at large W_b is 0.1 dB. The model errors for the H link and for the LOS channel are of the same order. This close agreement between the measurements and the proposed model illustrates the accuracy of our simple model relating the fade depth to channel bandwidth.

5 Conclusion

Experimental analysis of the indoor radio channel has been undertaken with the help of UWB frequency-domain channel measurements. A direct relationship between the channel bandwidth and fade depth has been proposed using an empirical treatment. According to our observations, the fade depth, in decibels, scales down approximately linearly with the logarithm of bandwidth up to 1 GHz, and is nearly constant thereafter. An empirical dual-slope model has been developed which accurately describes the dependence of fade depth on bandwidth, with a maximum error of 0.5 dB for the three-standard-deviation fade depth evaluation.

Our analysis indicates that most of the frequency diversity in the channel, which is directly related to fade depth, is extracted by the system as the bandwidth approaches 1 GHz. On this basis, it can be predicted that the diversity order improvement from a multiple-antenna diversity system will be much smaller in a wideband system than in a narrowband system, which is consistent with the results in [28, 30].

Some minor variations in the model parameters may be expected if the measurements are performed in different propagation environments, such as a large office space or an industrial environment. Thus the model parameters, k_i, $i = 1, 2, 3$, and critical bandwidth, W_0, may require some adjustment, but the overall trends, and indeed the model itself, are expected to remain valid. Our analysis has shown that the link polarisation or presence of LOS does not affect the fade depth significantly, especially in wideband and UWB channels. Further measurements to verify this formulation in other types of radio propagation environments will increase the value of this work.

doi: 10.1049/iet-map:20080015

6 Acknowledgments

This work was supported in part by the ESU Lindemann Trust and the UK Engineering and Physical Sciences Research Council Grant GR/T21769/01.

7 References

[1] RAPPAPORT T.S.: 'Wireless communications: principles and practice' (Prentice-Hall, 2001, 2nd edn.)

[2] JAKES W.C.: 'Microwave mobile communications' (Wiley, New York, 1974)

[3] SEKINE M., MAO Y.: 'Weibull radar clutter' (Institution of Engineering and Technology, London, UK, 1990)

[4] CHOI S.H., SMITH P.J., ALLEN B., MALIK W.Q., SHAFI M.: 'Severely fading MIMO channels: models and mutual information'. Proc. IEEE Int. Conf. Commun. (ICC), Glasgow, UK, June 2007

[5] ALLEN B., DOHLER M., OKON E.E., MALIK W.Q., BROWN A.K., EDWARDS D.J. (EDS.): 'Ultra-wideband antennas and propagation for communications, radar and imaging' (Wiley, London, UK, 2006)

[6] MOLISCH A.F.: 'Ultrawideband propagation channels – theory, measurement, and modeling', *IEEE Trans. Veh. Technol.*, 2005, **54**, (5), pp. 1528–1545

[7] KEIGNART J., DANIELE N.: 'Channel sounding and modelling for indoor UWB communications'. Proc. Int. Workshop Ultra Wideband Sys., Oulu, Finland, June 2003

[8] ALVAREZ A., VALERA G., LOBEIRA M., TORRES R.P., GARCIA J.L.: 'New channel impulse response model for UWB indoor system simulations'. Proc. IEEE Veh. Technol. Conf., Jeju, Korea, April 2003

[9] SCHUSTER U.G., BÖLCSKEI H., DURISI G.: 'Ultra-wideband channel modeling on the basis of information-theoretic criteria'. Proc. IEEE Int. Symp. Inf. Theory, Adelaide, Australia, September 2005

[10] HAYAR A.M., KNOPP R., SAADANE R.: 'Subspace analysis of indoor UWB channels', *EURASIP J. Appl. Signal Process*, 2005, **3**, pp. 287–295

[11] STÜBER G.L.: 'Principles of mobile communications' (Kluwer, Norwell, MA, USA, 2001, 2nd edn.)

[12] CORDOSO F.D., CORREIA L.M.: 'Fading depth dependence on system bandwidth in mobile communications – an analytical approximation', *IEEE Trans. Veh. Technol.*, 2003, **52**, (3), pp. 587–594

[13] OLSEN R.L., TJELTA T.: 'Worldwide techniques for predicting the multipath fading distribution on terrestrial LOS links: background and results of tests', *IEEE Trans. Antennas Propag.*, 1999, **47**, (1), pp. 157–170

[14] BARNETT W.T.: 'Multipath propagation at 4, 6, and 11 GHz', *Bell Syst. Tech. J.*, 1972, **51**, (2), pp. 321–361

[15] WILSON P., PAPAZIAN P., COTTON M., LO Y.: 'A comparison of 1920-MHz mobile channel diversity gain using horizontal and vertical arrays', *IEEE Trans. Commun.*, 2001, **49**, (12), pp. 2068–2070

[16] SKLAR B.: 'Rayleigh fading channels in mobile digital communication systems, part I: characterization', *IEEE Commun. Mag.*, 1997, **35**, (9), pp. 90–100

[17] CRAMER R.J.-M., SCHOLTZ R.A., WIN M.Z.: 'Evaluation of an ultra-wide-band propagation channel', *IEEE Trans. Antennas Propag*, 2002, **50**, (5), pp. 561–570

[18] Federal Communications Commission: 'Revision of Part 15 of the Commission's rules regarding ultra-wideband transmission systems: first report and order'. Federal Communications Commission, USA, Washington, DC, USA, Tech. Rep. FCC 02-48, February 2002

[19] HASHEMI H.: 'The indoor radio propagation channel', *Proc. IEEE*, 1993, **81**, (7), pp. 943–968

[20] TSE D., VISWANATH P.: 'Fundamentals of wireless communication' (Cambridge University Press, Cambridge, UK, 2005)

[21] CICCOGNANI W., DURANTINI A., CASSIOLI D.: 'Time domain propagation measurements of the UWB indoor channel using PN-sequence in the FCC-compliant band 3.66 GHz', *IEEE Trans. Antennas Propag.*, 2005, **53**, (4), pp. 1542–1549

[22] PAGANI P., PAJUSCO P.: 'Experimental assessment of the UWB channel variability in a dynamic indoor environment'. Proc. IEEE Int. Symp. Pers. Indoor Mobile Radio Commun., Barcelona, Spain, September 2004

[23] ROY S., FOERSTER J.R., SOMAYAZULU V.S., LEPER D.G.: 'Ultrawideband radio design: the promise of high-speed, short-range wireless connectivity', *Proc. IEEE*, 2004, **92**, (2), pp. 295–311

[24] MALIK W.Q., EDWARDS D.J., STEVENS C.J.: 'Angular-spectral antenna effects in ultra-wideband communications links', *IEE Proc. Commun.*, 2006, **153**, (1), pp. 99–106

[25] BATRA A., BALAKRISHNAN J., DABAK A., *ET AL.*: 'Multiband OFDM physical layer proposal for IEEE 802.15 Task Group 3a'. IEEE, Tech. Rep. P802.15-03/268r0-TG3a, July 2003

[26] PAGANI P., PAJUSCO P.: 'On the fading properties of a UWB link in a dynamic environment'. Proc. Eur. Electromagnetics Symp., Magdeburg, Germany, July 2004

[27] TARIQUE Z., MALIK W.Q., EDWARDS D.J.: 'Bandwidth requirements for accurate detection of direct path in multipath environment', *Electon. Lett*, 2006, **42**, (2), pp. 100–102

[28] MOLISCH A.F., STEINBAUER M., TOELTSCH M., BONEK E., THOM R.S.: 'Capacity of MIMO systems based on measured wireless channels', *IEEE J. Sel. Areas Commun.*, 2002, **20**, (3), pp. 561–569

[29] MALIK W.Q.: 'MIMO capacity convergence in frequency-selective channels', *IEEE Trans. Commun.*, 2008, To be published

[30] PAULRAJ A.J., NABAR R., GORE D.: 'Introduction to space-time wireless communications' (Cambridge University Press, Cambridge, UK, 2003)

[31] PAGANI P., PAJUSCO P.: 'Modeling the space- and time-variant ultra-wideband propagation channel'. Proc. IEEE Int. Conf. Ultra-Wideband, Waltham, MA, USA, September 2006

doi: 10.1049/iet-map:20080015